1 **Fracturing and crystal plastic behaviour of garnet under seismic stress in the**

2 **dry lower continental crust (Musgrave Ranges, Central Australia)**

5 Friedrich Hawemann[1*], Neil Mancktelow[1], Sebastian Wex[1], Giorgio Pennacchioni[2], Alfredo

6 Camacho[3]

7 1) Department of Earth Sciences, ETH Zurich, CH8092 Zurich, Switzerland

8 2) Department of Geosciences, University of Padova, Padova, Italy

9 3) Department of Geological Sciences, University of Manitoba, Winnipeg, Manitoba, R3T

10 2N2, Canada

11 * corresponding author friedrich.hawemann@erdw.ethz.ch

13 **Highlights**

14 • garnet deformed by fracturing and crystal-plasticity under dry lower crustal conditions

15 • Ca-diffusion profiles indicate multiple generations of fracturing

16 • diffusion is promoted along zones of higher dislocation density

17 • fracturing indicates transient high-stress (seismic) events in the lower continental

18 crust

19 **Abstract**

20 Garnet is a high strength mineral compared to other common minerals such as quartz and

21 feldspar in the felsic crust. In felsic mylonites, garnet typically occurs as porphyroclasts that

22 mostly evade crystal-plastic deformation, except under relatively high temperature

23 conditions. The microstructure of granulite facies garnet in felsic lower-crustal rocks of the

24 Musgrave Ranges (Central Australia) records both fracturing and crystal-plastic deformation.

25 Granulite facies metamorphism at ~ 1200 Ma generally dehydrated the rocks and produced

26 mm-sized garnets in peraluminous gneisses. A later ~ 550 Ma overprint under sub-eclogitic

27 conditions (600-700 °C, 1.1-1.3 GPa) developed mylonitic shear zones and abundant

28 pseudotachylyte, coeval with the neocrystallization of fine-grained, high-calcium garnet. In

29 the mylonites, granulite-facies garnet porphyroclasts are enriched in calcium along rims and

30 fractures. However, these rims are locally narrower than otherwise comparable rims along

31 original grain boundaries, indicating contemporaneous diffusion and fracturing of garnet. The

32 fractured garnets exhibit internal crystal-plastic deformation, which coincides with areas of

33 enhanced diffusion, usually along zones of crystal lattice distortion and dislocation walls

34 associated with subgrain rotation recrystallization. Fracturing of garnet under dry lower

35 crustal conditions, in an otherwise viscously flowing matrix, requires transient high

36 differential stress, most likely related to seismic rupture, consistent with the coeval

37 development of abundant pseudotachylyte.

38

41 **1 Introduction**

42 A fundamental problem in geology is the limited preservation of processes in the rock record.

43 This is especially the case for transient events, like earthquakes, traces of which are hardly

44 preserved due to later reworking. The best indicators for seismicity in the rock record are

45 pseudotachylytes (Sibson, 1975; Toy et al., 2011), although not every seismic event produces

46 frictional melts and, once formed, ductile creep or later brittle fracturing may erase most

47 traces (Sibson and Toy, 2006; Kirkpatrick and Rowe, 2013).

48 Garnet is stable in many metamorphic rocks over a large part of the pressure-temperature

49 space, is commonly preserved, and is suitable for a range of geothermobarometers and

50 geochronometers and their combination for geospeedometry (Lasaga, 1983; Caddick et al.,

51 2010; Baxter and Scherer, 2013). Being a high strength mineral (Karato et al., 1995; Wang and

52 Ji, 1999), both brittle and crystal plastic deformation are rarely observed in garnet when

53 compared to the common matrix minerals of the crust, such as quartz and feldspar. However,

54 Dalziel and Bailey (1968) already interpreted elongate garnets in high grade mylonites to be

55 the result of crystal plastic behaviour and advancements since then in electron microscopy,

56 and especially EBSD (electron backscatter diffraction), have allowed detailed investigation of

57 garnet textures (Kunze et al., 1993; Prior et al., 2000, 2002).

58 Experimental deformation of garnet indicates that differential stresses on the order of a few

59 GPa are required to produce shear fractures, and that the onset of crystal plastic behaviour

60 for strain rates typical of actively deforming regions ($10^{-12} - 10^{-15}$ s^{-1}; e.g. Behr and Platt, 2011)

61 should only occur at corresponding temperatures above ca. 750-640 °C (Karato et al., 1995;

62 Wang and Ji, 1999). The observation of fractured garnets in natural samples may therefore

63 be linked to seismic stresses, as suggested by Austrheim et al. (1996), who described

64 fracturing of garnets during pseudotachylyte formation and fluid-assisted eclogitization of

65 granulites. Trepmann and Stöckhert (2002) also interpreted the microstructure of fractured

66 and offset garnets as evidence for syn-seismic loading and post-seismic creep. More recently,

both brittle (Austrheim et al., 2017; Engi et al., 2017; Angiboust etal., 2017; Giuntoli et al., 2018; Hawemann et al., 2018; Petley-Ragan et al., 2019) and associated crystal-plastic behaviour (Austrheim etal., 2017; Petley-Ragan et al., 2019) of garnet has been related to seismic events in lower continental crust or deeply subducted continental fragments. Papa et al. (2018) interpreted similar deep-seated dilatant fracturing of garnet immediately adjacent to pseudotachylyte to be related to thermal shock due to frictional heating rather than to damage associated with propagation of the seismic rupture. Konrad-Schmolke et al. (2007) described enhanced diffusion of Mg along subgrain boundaries in garnet (but not of slow diffusing elements, such as Ca, Ti and Y) from high pressure meta-granitoids of the deeply subducted Sesia Zone (Western Alps). However, in contrast to more recent studies in the Sesia Zone, which propose that precursor fracturing was crucial for dissolution–precipitation and diffusion processes in garnet (Engi et al., 2018; Giuntoli et al., 2018), they considered that there were no signs of crystal-plastic deformation in their garnet samples and concluded that a diffusion-induced dislocation migration and/or diffusion-induced recrystallisation process was responsible for development of the observed subgrain texture.

Garnets can retain their microstructure and chemical composition during retrograde deformation and metamorphism and can therefore preserve indicators for seismic events, which are otherwise possibly erased from the rock record.Here we present a study of garnet microstructures from lower crustal rocks of the Musgrave Block in Australia, which:

(1) illustrates the close association between brittle and crystal-plastic deformation of garnet under well-established pressure-temperature conditions;

(2) infers deformation mechanisms from the observed microstructure;

(3) explores the close link between deformation and diffusion in garnet;

4

90   (4) complements other independent observations indicating transient high stresses in the

91   lower crust.

92

93   **2   Geological setting**

94   2.1 Regional geology

95   The Musgrave Block is located in an intraplate position close to the centre of the Australian

96   continent (inset Fig. 1). Amalgamation of the different cratonic blocks took place during the

97   Musgravian Orogeny (1120-1200 Ma), which pervasively overprinted ca. 1550 Ma gneisses

98   (Gray, 1978; Camacho and Fanning, 1995). The Petermann Orogeny (~550 Ma) produced a

99   series of crustal-scale fault zones, most prominently the Woodroffe Thrust and the Mann

100   Fault (Collerson et al., 1972; Major, 1973; Bell, 1978; Camacho and Fanning, 1995; Raimondo

101   et al., 2010; Hawemann et al., 2018, 2019; Wex et al., 2017, 2018, 2019). The south-dipping

102   Woodroffe Thrust has a top-to-the-north sense of shear, and juxtaposes the Fregon

103   Subdomain in the south (hanging wall) against the Mulga Park Subdomain in the north

104   (footwall). During the Musgravian Orogeny, the Mulga Park Subdomain attained amphibolite

105   facies conditions while the Fregon Subdomain reached granulite facies (Camacho and

106   Fanning, 1995; Scrimgeour et al., 1999; Scrimgeour and Close, 1999), and depleted the rocks

107   of OH-bearing minerals (Wex et al., 2018; Hawemann et al., 2018).

108   The Woodroffe Thrust hosts one of the largest occurrences of pseudotachylyte worldwide

109   (Camacho et al., 1995), but all larger scale shear zones in the hanging wall also show abundant

110   pseudotachylyte that developed under lower crustal conditions (Camacho, 1997; Hawemann

111   et al., 2018). Deformation in the Fregon Subdomain associated with the Petermann Orogeny

112   is concentrated along the sub-eclogitic (~650 °C, 1.2 GPa) Davenport Shear Zone and the

113   North Davenport Shear Zone (Fig. 1), with little discernible overprint of the earlier granulites

114   in between (Camacho et al., 1997). The Davenport Shear Zone is a WNW-ESE-striking, strike-

115   slip zone, with a near horizontal stretching lineation. Deformation inside the Davenport Shear

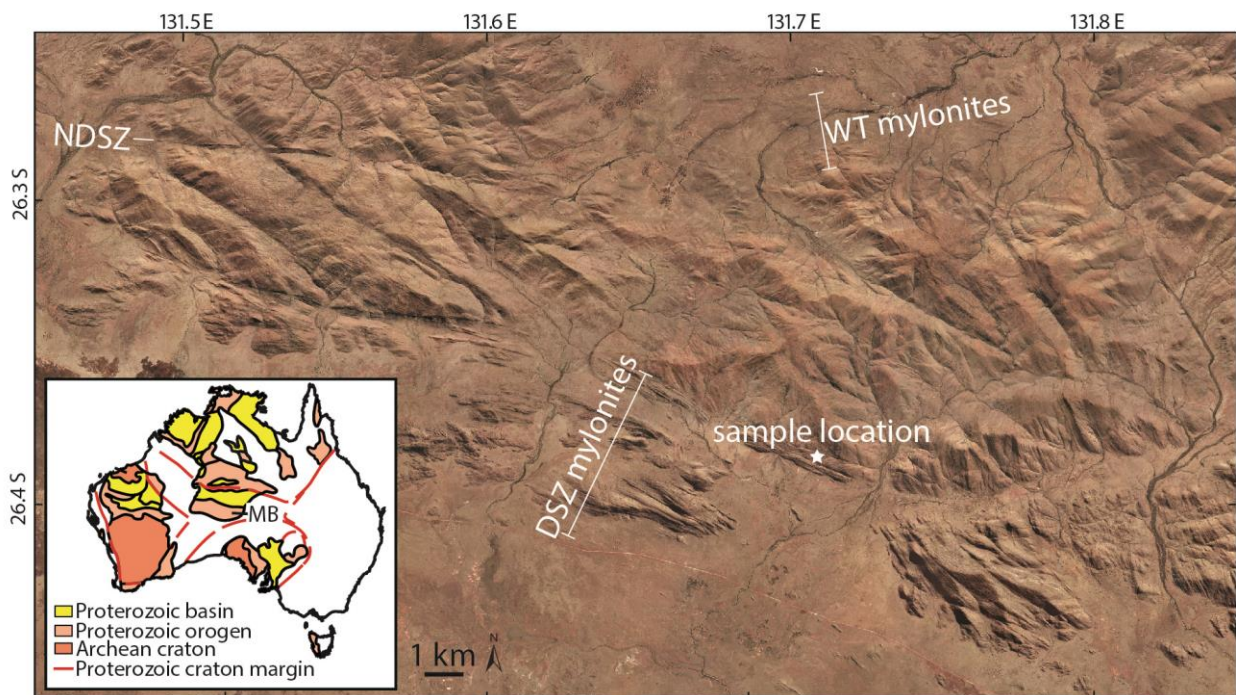116   Zone itself is heterogeneous and strongly localized (Hawemann et al., 2019).

117

118

Figure 1: Airborne imagery of the study area with sample location (26.3849 S, 131.7067 E) in the Davenport Shear Zone (DSZ). NDSZ = North Davenport Shear Zone, WT = Woodroffe Thrust. Image from the Department of Primary Industries and Regions, South Australia (PIRSA), 2012. Inset: Location of the Musgrave Block (MB) in between the amalgamated Australian Cratons. Modified after Evins et al. (2010)

119

120   2.2 Sample description

121   Fractured garnet is ubiquitous in the Fregon Subdomain and is not exclusively found in

122   association with pseudotachylyte veins. However, this study focuses on a representative

123   outcrop for which field relationships, metamorphic, and deformation conditions have been

124   well established (F68, Hawemann et al., 2018; 26.3849 S, 131.7067 E). This outcrop consists

6

125   of a quartzo-feldspathic mylonite with millimetre-sized, granulite facies garnets, and includes

126   multiple pseudotachylyte veins and breccias. Pseudotachylytes in the studied outcrop are

127   sheared, as indicated by elongated clasts (Fig. 2a, c), and show the same stretching lineation

128   as the host mylonite. The original discordant relationship to the host foliation is still

129   preserved, with the crosscutting relationship most obvious in sections perpendicular to the

130   stretching lineation (Fig. 2b).

131   The syn-mylonitic assemblage associated with the Petermann overprint of the felsic

132   granulites is Qz+Kfs+Pl+Gt+Bt+Ky+Ilm+Rt (mineral abbreviations following Whitney and

133   Evans, 2010), and is similar to that of the associated sheared pseudotachylyte

134   (Qz+Kfs+Pl+Gt+Bt+Ky+Rt) (Hawemann et al., 2018). The fine-grained garnet growing within

135   the pseudotachylyte gives the rock its macroscopic caramel-colour (Fig. 2). Larger fractured

136   garnets within the granulites are clearly recognizable in polished hand specimens (Fig. 2c) and

137   are very apparent in thin section (Fig. 3). The metamorphic conditions during shearing of this

138   pseudotachylye are estimated at ~600 °C and ~1.1 GPa (Fig. 7 of Hawemann et al., 2018).
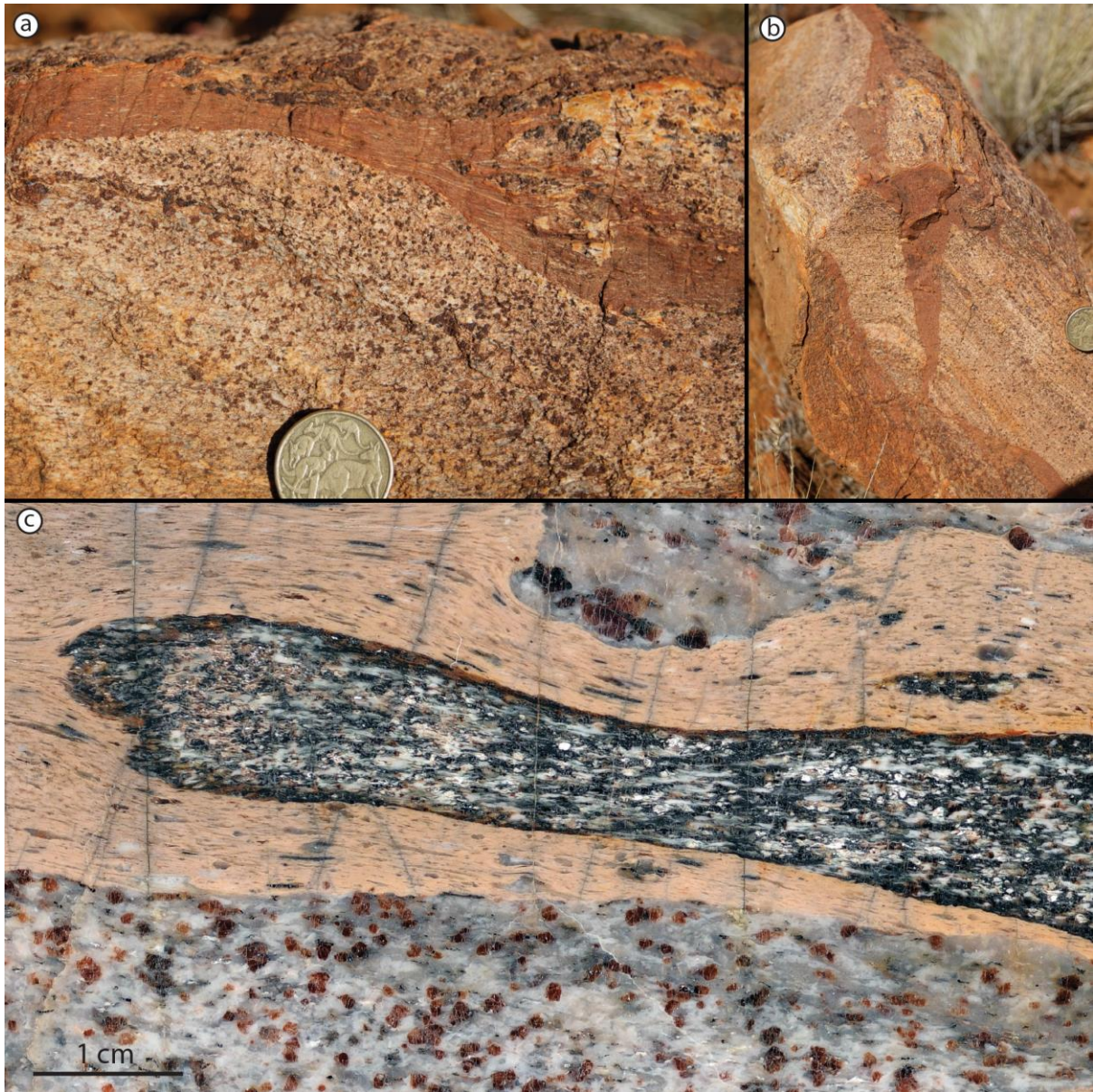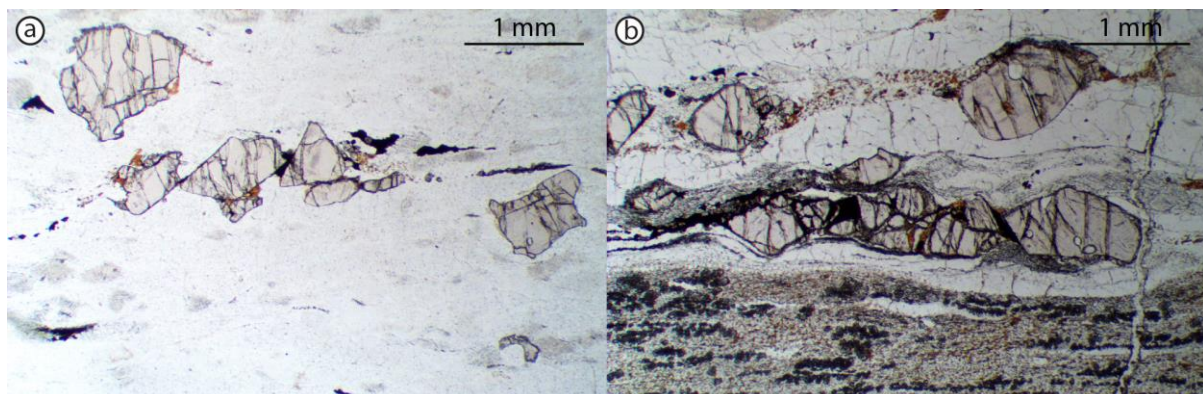
139

140

Figure 2: Sheared pseudotachylyte in a view orthogonal to the foliation of host felsic mylonite, and looking perpendicular (a) and parallel (b) to the stretching lineation. c) Polished hand specimen of a sheared pseudotachylyte breccia with the caramel-coloured foliated pseudotachylyte matrix including elongated clasts and an elongate fragment of mafic granulite. The host rock shows millimetre-sized garnets with fractures. Plane of the polished surface is perpendicular to the foliation and parallel to the stretching lineation.

141

3   Garnet microstructure and compositional variation

3.1 Optical microstructure

Granulite facies garnet porphyroclasts in Musgravian peraluminous gneisses mylonitized during the Petermann Orogeny are almost invariably fractured, irrespective of their proximity to pseudotachylyte (Fig. 3). Large garnet porphyroclasts (>1 mm) are typically slightly elongated with their long axis parallel to the foliation, which is attributed at least partially to resorption. Fractures in garnets often show offsets on the order of a few 100 µm. It is not possible to determine whether these offsets are primarily due to the initial shear fracture or result from subsequent sliding during ongoing ductile shear. Moreover, no consistent sense of shear can be derived from the offsets (Fig. 3a, b). These discrete fractures are sub-planar, commonly have a consistent orientation at a moderate angle to the foliation, and locally occur in conjugate sets (Fig. 3b). Wide fractures are filled with biotite, kyanite and quartz (Fig. 4b). A later generation of unfilled fractures, without any discernible offset, is oriented perpendicular to both the foliation and stretching lineation (Fig. 3b). Garnet porphyroclasts commonly contain rutile exsolution lamellae and inclusions of monazite and kyanite (Fig. A1). The latter are present as aggregates with an overall prismatic shape, possibly representing pseudomorphs after sillimanite (Camacho and Fitzgerald, 2010).

161

162

163

164   ## 3.2 Analytical techniques

165   Quantitative mineral compositions were measured with a JEOL JXA-8200 electron probe

166   micro-analyzer (EPMA), equipped with a tungsten filament, at the Institute of Geochemistry

167   and Petrology at ETH Zurich (Switzerland). Natural standards were used for quantification,

168   and, when available, natural garnet standards were preferred. To reach a spatial resolution

169   of about 1 μm, an acceleration voltage of 10 kV was set (Fig. 8 in Hofer and Brey, 2007).

170   Elemental maps were acquired using energy wavelength-dispersive spectrometers in parallel

171   for calcium, to increase the signal-to-noise ratio. Backscatter electron images (BSE), energy-

172   dispersive spectrometry (EDS) and electron backscatter diffraction (EBSD) mapping was

173   carried out on a Quanta 200F field emission gun (FEG) scanning electron microscope at the

174   ScopeM (Scientific Center for Optical and Electron Microscopy, ETH Zurich). EBSD maps were

175   collected with an acceleration voltage of 20 kV, a sample tilt of 70° and a working distance of

176   15 mm. Data were post-processed using chemical indexing with the software OIM 7 by EDAX.

177   When necessary, three different clean-up techniques were used: neighbour confidence index

178   correlation, neighbour orientation correlation and grain dilation. Point and map analyses, as

179   well as BSE images, were combined for correlation with optical microscope images in a QGIS-

180   project (Open Source Geospatial foundation). Two lamellae were cut with a focused ion beam

181   (FIB) for transmission electron microscopy (TEM). The microscope used for TEM is a Tecnai

182   F30 with a FEG source operated at 300 kV and equipped with a Gatan 794 MultiScan CCD

183   (ScopeM, ETH Zurich).

184   3.3 Compositional gradients

185   Granulite facies garnet has a homogeneous composition of X_{Alm} 0.54, X_{Pyp} 0.40, X_{Grs} 0.03, X_{Sps}

186   0.03, whereas garnet neocrystallized during the Petermann Orogeny is more Ca-rich (X_{Alm}

187   0.48, X_{Pyp} 0.28, X_{Grs} 0.22, X_{Sps} 0.02). Grain boundaries of granulite facies garnet and fractures

188   are decorated with a Ca-enriched rim, 20 to 40 µm wide (Fig. 4c). The length-scale for

189   variation in Fe (X_{Alm}) and Mg (X_{Pyp}) is identical to that for Ca (X_{Grs}), whereas the Mn content

190   (X_{Sps}) does not show any variation (Fig 4d). Neocrystallized garnet is present where the grain

191   boundary is in contact with, or close to, plagioclase. The outermost rim of remnant garnet has

192   the same composition as the neocrystallized garnet (Fig. 4d, profile 1). The granulite-facies

193   plagioclase is partially transformed to a more Na-rich plagioclase with needle shaped

194   inclusions of kyanite (bottom of Fig. 4e). This reaction provides Ca for the observed diffusion

195   into garnet (Camacho et al., 2009).

196   Along fractures across the porphyroclasts, the Ca enrichment is narrower than along the grain

197   boundaries and the grossular component only reaches up to about X_{Grs} 0.1 (Fig. 4d, profile 2).

198   Compositional gradients are also present around inclusions in garnet connected to the outer

199   garnet boundary, providing evidence of Ca diffusion along grain boundaries (right part of Fig.

200   4c, profile 3 in Fig 4d). Profile 4 (Fig. 4d) was measured next to a kyanite inclusion: the

201   diffusion length is still comparable to those of profiles 1-3, but Ca concentrations are much

202   lower. Ca probably diffused along fractures (invisible in the plane of the thin section) towards

203   the inclusion. In summary, the diffusion length at the original grain boundaries is maximized

204   where in contact with plagioclase, and otherwise constant at about 20 µm width. However,

205   variations in diffusion lengths do occur around garnet fragments, without any correlation with

206   the proximity to plagioclase, although the exact relationship in the third dimension is

207   unknown. Surfaces with limited diffusion can often be identified as fracture surfaces, which

208   were exposed to diffusion for a shorter time than original grain boundaries (Fig. 4e). Fractures

209   oriented perpendicular to the foliation and stretching lineation lack any signs of diffusion and

210   are therefore interpreted as later stage extensional fractures.

211   Some garnets display more complicated compositional patterns, with zones >100 µm of Ca

212   enrichment extending into the porphyroclast's interior, which are not associated with

213   fractures (e.g. the garnet fragment on the far right in Figure 4e). EBSD analysis highlights that

214   the three fragments in the right part of Figure 4e most likely originated from the same grain,

215   as they share a common rotation axis (Fig. 4f). The colours in the inverse pole figure map are

216   not solid, reflecting slight variations of orientation within the crystal. Furthermore, the image

217   quality map shows areas of suppressed Kikuchi patterns (grey value) suggestive of higher

218   dislocation density and therefore possible subgrain boundaries (Fig. 4f). The misorientation

219   angle map (Fig. 4g) reveals a complex pattern of varying crystal orientation (all within the

220   order of 5°) in the fragments, with very distributed zones connected to the edges of the

221   crystal, triangular-shaped zones of misorientation (upper left of Fig. 4g), and discrete zones

222   (lower right of Fig. 4g). The discrete zones of misorientation, about 5 µm wide, correlate well

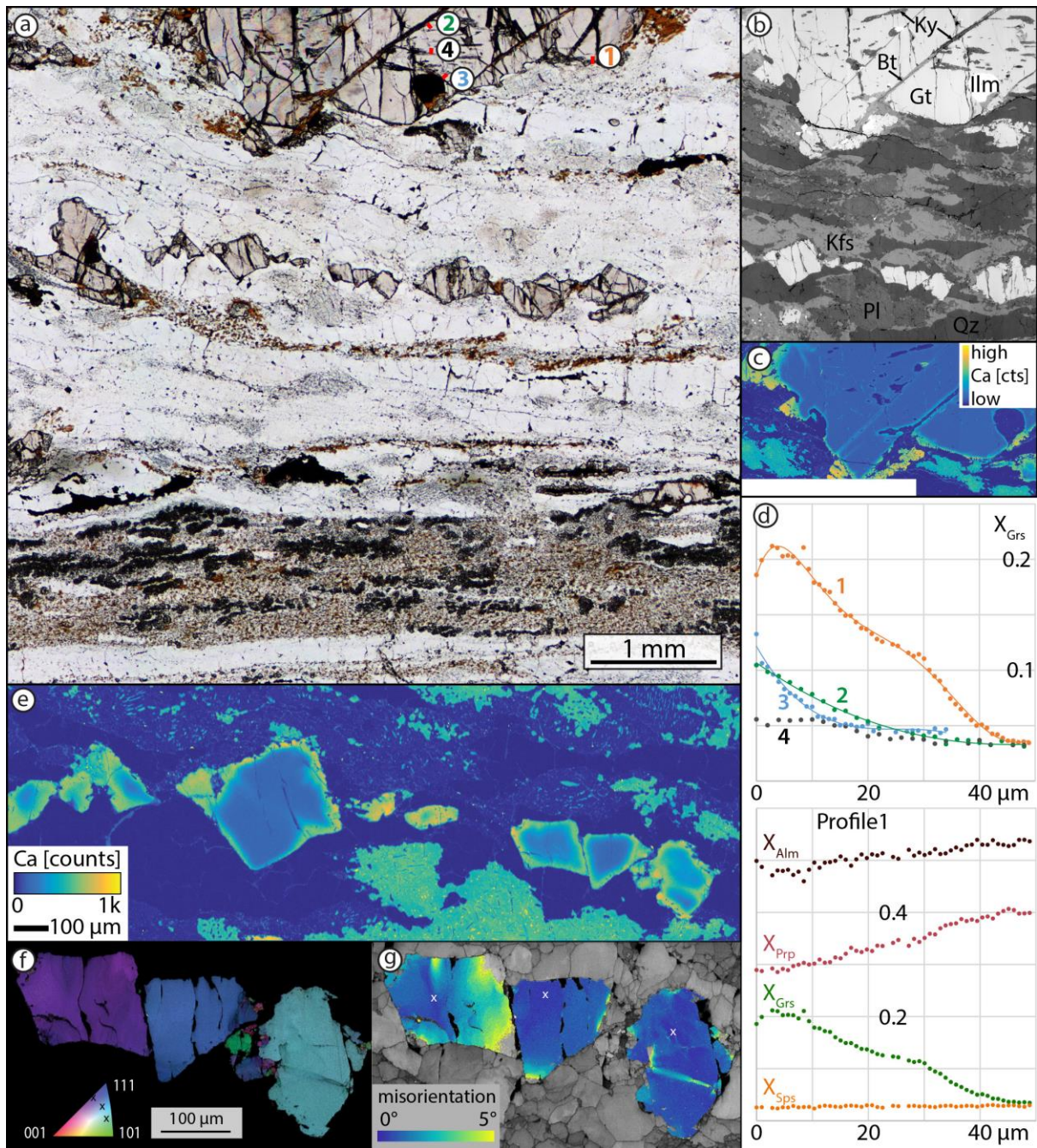223   with the Ca-enriched zones (compare Fig. 4e, f, garnet fragment on the right).

224

Figure 4: a) Plane polarized light image of thin section with fractured garnets and a pseudotachylyte vein in the lower part of the image. b) BSE image of the upper area of (a), with same scale as (a). c) EPMA X-ray map for Ca reveals an enrichment in thin gradational rims along grain boundaries and fractures, and within neocrystallized garnet (euhedral, orange). d) Grossular component profiles indicated on (a) (profile lines are not to scale for the sake of visibility) and compositional profiles for four garnet end-members in profile 1. e) EPMA X-ray map for Ca for the garnet fragments in the center of (a). Note the uneven colours in the plagioclase and the blue kyanite needles. f) Inverse pole figure map with superimposed image quality map for garnet fragments shows a common rotation pole. g) Misorientation map relative to reference point for each fragment reveals internal lattice distortions.

225

226   3.4 Texture of deformed garnets

227   Two to three orientations of fractures are generally present in a single garnet crystal and

228   coincide with the trace of the (101)-plane derived from EBSD data (Fig. 5a, b). Fracture set (I)

229   in the example of Figure 5a is often associated with a relative rotation of both sides, as visible

230   from the difference in colour. In the lower part of the grain, where the fracture density is very

231   high, more subgrains are present. The subgrain spatial density increases towards the original

232   grain boundary and some subgrains are "eroded" by ductile shearing and strung out along the

233   foliation. This demonstrates that ductile shearing outlasted subgrain formation and

234   fracturing. The fractures described above are all crosscut by extensional fractures (set II in Fig.

235   5a), oriented perpendicular to the stretching lineation and foliation, which do not show any

236   associated distortion of the crystal lattice.

237   The garnet porphyroclast of Figure 5c shows a central fracture as well as a set of two other

238   parallel fractures. The central fracture is the only one with significant offset and is filled with

239   kyanite and quartz. This fracture displays misorientations of more than 5° towards the right-

240   hand side of the scan, but none towards the left-hand side. In the lower left corner of the

241   fragment, subgrains are observed with misorientations, relative to the average orientation,

242   typically in the range of 10°. Misorientation axes are often parallel to (111) and (101). The

243   lowermost fragment shows a wide zone of progressive rotation. The chemical profile in Figure

244   5e shows the highest Ca counts towards the boundaries of the porphyroclasts and, internally,

245   towards two fractures. The larger fracture with apparent offset of the two garnet fragments

246   exhibits a less well-developed zone of Ca enrichment when compared to the tight fracture

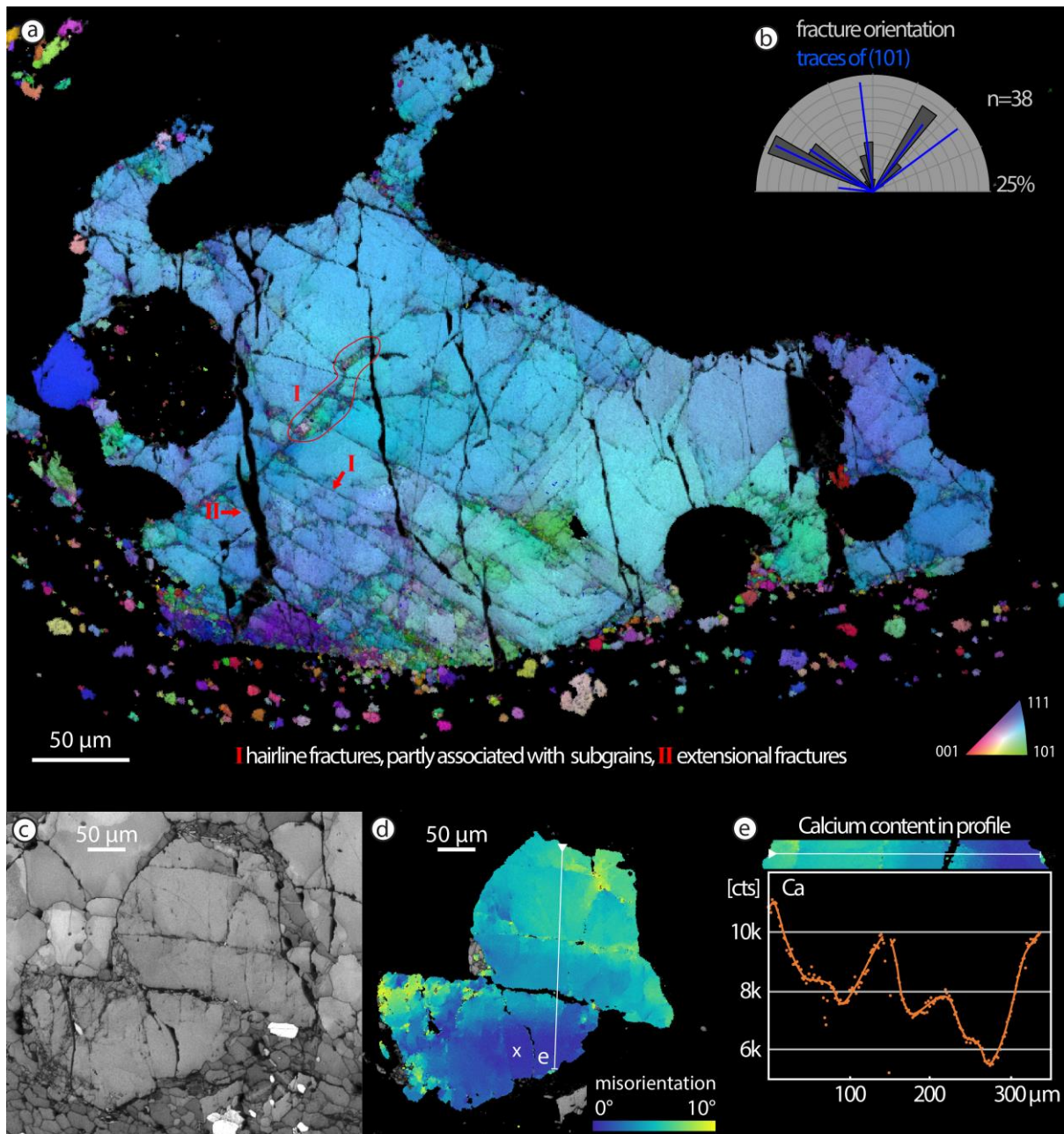247   with introduced lattice distortion.

Figure 5: a) Inverse pole figure map of fractured garnet with three dominant orientations of fractures. b) Rose diagram correlating traced fracture orientations and (101)-planes for garnet in (a). c) Image quality map of a fragmented garnet with subgrains. d) Misorientation plot (with respect to the point marked with the white x) shows long wavelength bending in the lower fragment and distortion in the crystal lattice induced by a fracture in the upper fragment. e) EDS-calcium counts for the profile marked as a thin white line in (d).

251   3.5 TEM investigations

252   The garnet fragment of Figure 4g was further investigated using TEM, as it includes a narrow

253   zone of misorientation without fractures and is therefore suitable for preparation of FIB-

254   lamellae. As visible in Figure 6a (around profile 1), the image quality map shows a well-defined

255   narrow, darker grey band, possibly indicating high dislocation density. The zone is even more

256   evident in the misorientation plot (Fig. 6b) and changes from about 5 µm wide, with discrete

257   boundaries to the right, to a wider (> 10 µm) band towards the left of the image. In the upper

258   left part of the image, a subgrain boundary with > 5° misorientation transitions into a zone of

259   gradual misorientation. The misorientation axis is consistently parallel to (101) with minor

260   rotation around (111) (Fig. 6c, Fig. A2). Misorientation profiles reveal a slight asymmetry

261   within the narrow band, where the lower boundary appears to be sharper. Misorientation

262   changes more gradually within the wider portion of the misorientation band. Locally,

263   subgrains developed with discrete boundaries, documenting a misorientation of usually

264   around 5-10° (profile 3 in Fig. 6d). The FIB-lamella was cut across the narrow band of

265   misorientations (Fig. 6e). The lower boundary corresponds to a narrow discrete zone, without

266   visible dislocations (Fig. 6f). The upper boundary is marked by a series of dislocation walls and

267   only a few free dislocations are visible, which are often organized in arrays (Fig. 6g, h). The

268   existence of dislocation walls and subgrain boundaries indicates recovery by dislocation climb

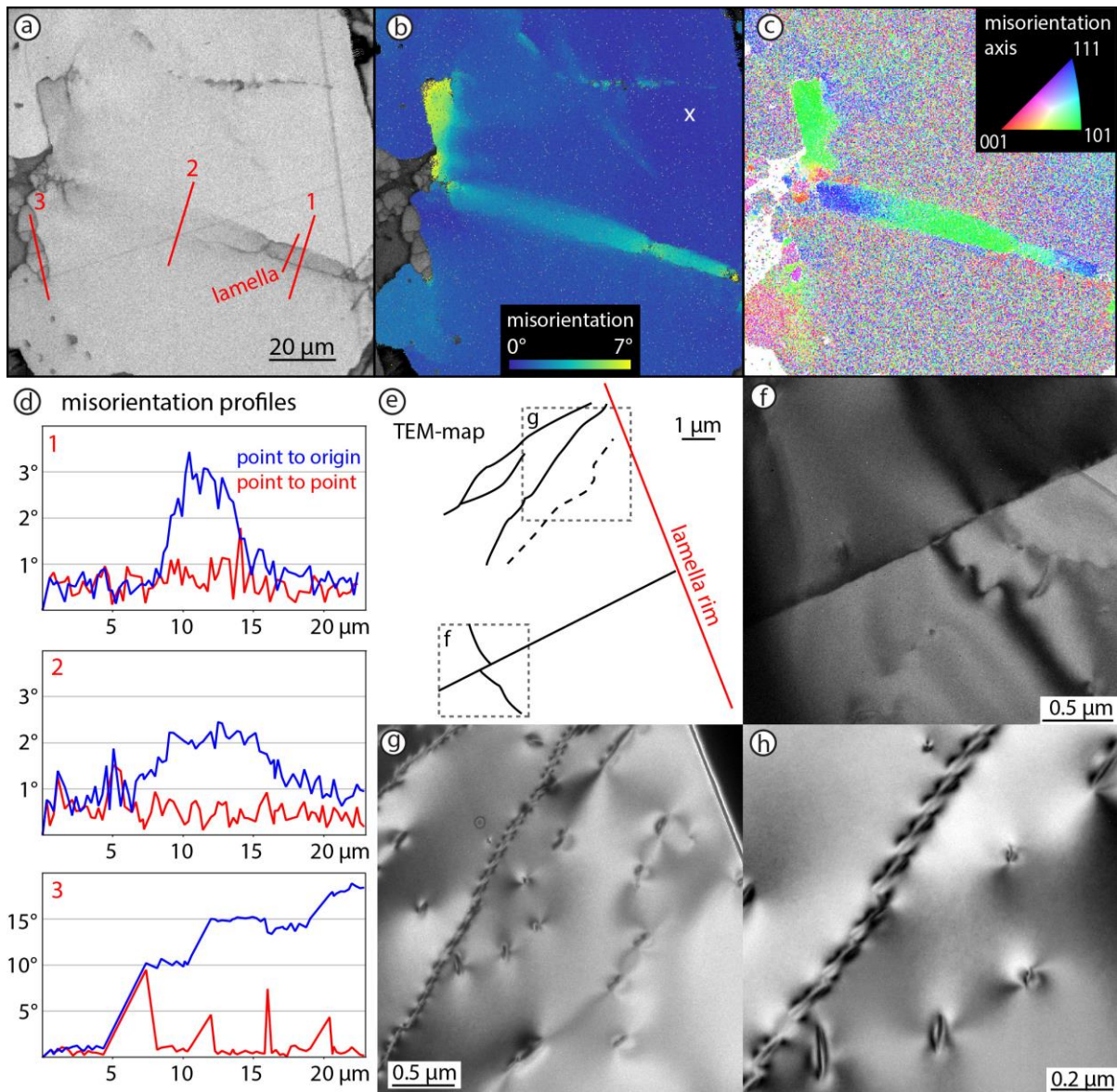269   (e.g., Hobbs, 1968; Passchier and Trouw, 2005).

270

Figure 6: a) Image quality map of the garnet fragment (compare Fig. 4f) with darker zones that can be interpreted as areas of high dislocation density and location of the FIB-lamella. b) Misorientation plot with respect to the reference point (marked with the white x) shows a discrete zone of misorientation, which has discrete boundaries in the right part of the image, but is more distributed towards the left. c) Misorientation axis plot with respect to the average orientation of the grain shows a consistent rotation around the (101) and (111) axes. For pole figure plots, see Fig. A2. d) Misorientation profiles indicated in a), for (1) the narrow zone, (2) the more distributed zone and (3) for subgrains. e) Overview sketch of the FIB-lamella used for TEM-analysis for correlation with the EBSD data. f) Sharp contrast boundary in the lower part of the lamella. g) Two dislocation walls with a few free dislocations, which are partly linking up parallel to the dislocation walls. h) Detail of the centre of (g)

271

272

4   Discussion

Garnets in this study show evidence for both brittle and ductile deformation under relatively low temperatures of about 600 °C, as inferred from synchronous diffusion and ductile shearing of pseudotachylyte (Hawemann et al, 2018). This is below the experimentally determined values for the onset of crystal-plastic deformation of garnet (Wang and Ji, 1999) at the higher strain rates considered typical of mylonitic shear zones (> 10^{-14} s^{-1}). In contrast to experiments, many natural examples (Vollbrecht et al., 2006; Bestmann et al., 2008; Austrheim et al., 2017) indicate crystal plasticity of garnet at lower temperatures between 650 °C and 700 °C.

The presence of microstructures and textures consistent with dislocation climb and recovery, as well as subgrain rotation, in garnet at around 600 °C is in agreement with previous studies (Bestmann et al., 2008; Massey et al.,2011). No evidence for grain boundary sliding is observed, since subgrains show rotation around a specific crystallographic axis. Rotation around (111) and (101) is in accordance with the slip systems described by Voegelé et al. (1998).

Multiple generations of overprinting fractures with different orientation demonstrate repeated fracturing events. Extensional fractures do not show any induced lattice distortion or diffusion and therefore occurred after the temperature had decreased to values too low for diffusion (Camacho et al., 2009), possibly during exhumation (compare Prior, 1993 and Ji et al., 1997).

In contrast to the observations of Austrheim et al. (2017), Papa et al. (2018) and Petley-Ragan et al. (2019) from other examples in the deep continental crust, no "explosive fracturing", "shattering" or "fragmentation" of garnet is observed in relict porphyroclasts immediately

296   adjacent to pseudotachylyte. The fractures described here are generally planar and often

297   consistently oriented, in some cases showing single and conjugate shear offsets. Fractured

298   garnet is not restricted to the boundary with pseudotachylyte and is still present even in

299   samples without pseudotachylyte, where the nearest pseudotachylyte is possibly many

300   metres or more away. Fracturing in this case cannot be related to thermal shock (Papa et al.,

301   2018) or localized high stress due to (seismic) fracture propagation (Austrheim et al., 2017;

302   Petley-Ragan et al., 2019), but must reflect a larger scale distribution of differential stresses

303   in the lower crust that were, at least transiently, high enough to cause brittle garnet failure

304   (Hawemann et al., 2019). This could be due to stress pulses from earthquakes in the shallower

305   brittle regime (Trepmann and Stöckhert, 2002; Ellis and Stöckhert, 2004; Jamtveit et al.,

306   2018a, b; Jamtveit et al., in press) or a more local, lower crustal source due to jostling of less-

307   deformed strong blocks within an irregular shear zone network (Hawemann et al., 2019).

308   The narrower Ca diffusion profiles on some fractures relative to garnet rims and crosscutting

309   relationships suggest that fracturing was recurrent under sub-eclogite facies metamorphic

310   conditions, as also indicated by the occasional presence of kyanite in some fractures. The

311   presence of kyanite needles and the absence of zoisite/clinozoisite or epidote, as a

312   breakdown product of plagioclase during sub-eclogitic metamorphism (Fig. 3b), indicate

313   relatively dry lower crustal conditions (Hawemann et al., 2018). According to Wayte et al.

314   (1989), this indicates a water activity of < 0.004, calculated for rocks of comparable

315   composition and P-T conditions. However, new biotite did form in fractures across relict

316   garnet, so conditions were probably not strictly anhydrous. The sheared and recrystallized

317   pseudotachylyte developed a similar synkinematic assemblage as the host mylonite,

318   demonstrating that there is also no marked partitioning of water into the frictional melt,

319   which implies little free or bound water available in the original source rock (e.g. Wex et al.,

320   2018). The effect of pore-fluid pressure on the effective confining pressure must therefore

321   have been negligible.

322   As reported in Hawemann et al. (2019), the dynamically recrystallized quartz grain size and

323   microstructure in the host rock mylonites indicates that long-term flow stresses were not

324   particularly high, on the order of less than 10 MPa. The ambient pressure of ca. 1.1-1.2 GPa

325   determined for the host rocks should therefore be close to the lithostatic value (Mancktelow,

326   2008). Figure 7 shows a simple linear plot of the Mohr-Coulomb failure criterion for an angle

327   of internal friction of 30° (coefficient μ = 0.6), a lithostatic load of 1.2 GPa, and no pore fluid

328   pressure. This plot is only qualitative, since the angle of internal friction could decrease

329   towards higher pressure (Shimada et al., 1983). However, the summary of experimental

330   results in Byerlee (1978) indicates that there may be little change at least up to pressures

331   similar to those considered here. It follows that the differential stress for fracture initiation

332   must have been of the same order as the confining pressure (Fig. 7). As discussed in detail in

333   Hawemann et al. (2019), such high differential stresses, leading to garnet fracture and the

334   development of abundant pseudotachylyte, can only have been transient and presumably

335   related to repeated short-term seismic events in the lower continental crust (Hawemann et

336   al., 2018; Jamtveit et al, 2018a, b; Menegon et al., 2017). The lack of shattered garnet adjacent

337   to pseudotachylyte in these samples may reflect drier conditions relative to those in the

338   Bergen Arc (Austrheim et al., 2017) and Mont Mary (Papa et al., 2018). The samples studied

339   could therefore represent one end-member of the lower continental crust, where

340   deformation occurs without the initial presence or influx of free water during fracturing and

341   subsequent crystal-plastic deformation.
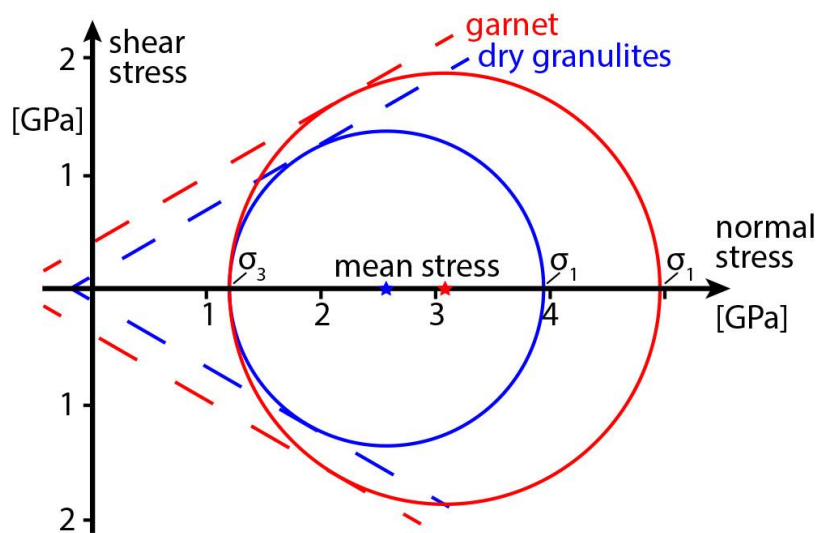
342

Figure 7: Mohr circles for fracturing of dry granulites and garnet at 1.2 GPa lithostatic load

5   Conclusions

In dry lower continental crust deformed under conditions of ca. 600 °C and 1.1 GPa, garnet shows both single and conjugate sets of shear fractures, fractures with associated subgrains and induced lattice damage around fractures, subgrain formation without fracturing, and late-stage extensional fractures. Most of these fractures show a strong crystallographic control, with fracturing preferentially occurring along the (101) planes of garnet. Dynamic recrystallization is evident from inferred subgrain rotation recrystallization and recovery is manifested by the presence of dislocation walls. The observed microstructures of garnets are interpreted to record transient high stresses during deep seismic events in the lower crustal Fregon Subdomain. This is also indicated by the abundant occurrence of pseudotachylyte developed under similar lower crustal conditions and, possibly, by the variability of recrystallized quartz grain sizes including values down to a few micrometres (Hawemann et al. 2009b). The studied example represents one end-member of lower continental crustal behaviour where, because of earlier metamorphic dehydration and the intracratonic position

359 well removed from the plate margin, rocks were initially dry and water was not introduced

360 during fracturing and crystal-plastic deformation.

361 **Author contributions**

362 All authors listed took part in at least two of the three field seasons. NM assisted FH in the data

363 collection and interpretation. AC's and GP's knowledge in the field of garnet deformation and diffusion

364 processes were crucial in preparing the manuscript. SW contributed to the microprobe and SEM work.

365 FH prepared the manuscript with contributions from all co-authors.

366 **Competing interests**

367 The authors declare that they have no conflict of interest.

368

369 **Acknowledgements**

382

Data Availability

384 All data used in this paper can be accessed through the depository of the Open Science

385 Framework here: https://osf.io/yrzgh/

386

References

388 Austrheim, H., Erambert, M. and Boundy, T. M.: Garnets recording deep crustal earthquakes, Earth
389 and Planetary Science Letters, 139(1–2), 223–238, doi:10.1016/0012-821X(95)00232-2, 1996.

390 Austrheim, H., Dunkel, K. G., Plümper, O., Ildefonse, B., Liu, Y. and Jamtveit, B.: Fragmentation of
391 wall rock garnets during deep crustal earthquakes, Science Advances, 3(2), e1602067,
392 doi:10.1126/sciadv.1602067, 2017.

393 Angiboust, S., Yamato, P., Hertgen, S., Hyppolito, T., Bebout, G.E., Morales, L.: Fluid pathways and
394 high-P metasomatism in a subducted continental slice (Mt. Emilius klippe, W. Alps), Journal of
395 Metamorphic Geology, 35, 471–492, 2017.

396 Baxter, E. F. and Scherer, E. E.: Garnet Geochronology: Timekeeper of Tectonometamorphic
397 Processes, Elements, 9(6), 433–438, doi:10.2113/gselements.9.6.433, 2013.

398 Behr, W.M., Platt, J.P.: A naturally constrained stress profile through the middle crust in an
399 extensional terrane. Earth and Planetary Science Letters 303, 181-192, 2011.

400 Bell, T. H.: Progressive deformation and reorientation of fold axes in a ductile mylonite zone: the
401 Woodroffe thrust, Tectonophysics, 44(1), 285–320, 1978.

402 Bestmann, M., Habler, G., Heidelbach, F. and Thöni, M.: Dynamic recrystallization of garnet and
403 related diffusion processes, Journal of Structural Geology, 30(6), 777–790,
404 doi:10.1016/j.jsg.2008.02.007, 2008.

405 Caddick, M. J., Konopasek, J. and Thompson, A. B.: Preservation of Garnet Growth Zoning and the
406 Duration of Prograde Metamorphism, Journal of Petrology, 51(11), 2327–2347,
407 doi:10.1093/petrology/egq059, 2010.

408 Camacho, A. and Fanning, C. M.: Some isotopic constraints on the evolution of the granulite and
409 upper amphibolite facies terranes in the eastern Musgrave Block, central Australia, Precambrian
410 Research, 71(1), 155–181, 1995.

411 Camacho, A. and Fitz Gerald, J. D.: Misidentification of oxide phases and of twinned kyanite:
412 implications for inferred P-T histories of the Musgrave Block, central Australia, Journal of the Virtual
413 Explorer, 35, doi:10.3809/jvirtex.2011.00275, 2010.

414 Camacho, A., Vernon, R. H. and Fitz Gerald, J. D.: Large volumes of anhydrous pseudotachylyte in the
415 Woodroffe Thrust, eastern Musgrave Ranges, Australia, Journal of Structural Geology, 17(3), 371–
416 383, 1995.

417 Camacho, A., Compston, W., McCulloch, M. and McDougall, I.: Timing and exhumation of eclogite
418 facies shear zones, Musgrave Block, central Australia, J. metamorphic Geol., 15, 735–751, 1997.

419 Camacho, A., Yang, P. and Frederiksen, A.: Constraints from diffusion profiles on the duration of
420 high-strain deformation in thickened crust, Geology, 37(8), 755–758, 2009.

421 Collerson, K. D., Oliver, R. L. and Rutland, R. W. R.: An example of structural and metamorphic
422 relationships in the Musgrave orogenic belt, central Australia, Journal of the Geological Society of
423 Australia, 18(4), 379–393, doi:10.1080/00167617208728776, 1972.

424 Dalziel, I. W. D. and Bailey, S. W.: Deformed garnets in a mylonitic rock from the Grenville Front and
425 their tectonic significance, American Journal of Science, 266(7), 542–562, doi:10.2475/ajs.266.7.542,
426 1968.

427 Ellis, S., Stöckhert, B.: Elevated stresses and creep rates beneath the brittle-ductile transition caused
428 by seismic faulting in the upper crust. Journal of Geophysical Research, 109, B05407, 2017.

429 Engi, M., Giuntoli, F., Lanari, P., Burn, M., Kunz, B. E., and Bouvier, A.-S.: Pervasive eclogitization due
430 to brittle deformation and rehydration of subducted basement: Effects on continental recycling?,
431 Geochemistry Geophysics Geosystems, 19, https://doi.org/10.1002/2017GC007215, 2018.

432 Evins, P. M., Smithies, R. H., Howard, H. M., Kirkland, C. L., Wingate, M. T. D. and Bodorkos, S.:
433 Redefining the Giles Event within the setting of the 1120-1020 Ma Ngaanyatjarra Rift, West
434 Musgrave Province, Central Australia, Geological Society of Western Australia, East Perth, W.A.,
435 2010.

436 Gray, C. M.: Geochronology of granulite‐facies gneisses in the western Musgrave Block, Central
437 Australia, Journal of the Geological Society of Australia, 25(7–8), 403–414,
438 doi:10.1080/00167617808729050, 1978.

439 Giuntoli, F., Lanari, P., and Engi, M.: Deeply subducted continental fragments – Part 1: Fracturing,
440 dissolution–precipitation, and diffusion processes recorded by garnet textures of the central Sesia
441 Zone (western Italian Alps), Solid Earth, 9, 167–189, https://doi.org/10.5194/se-9-167-2018, 2018.

442 Hawemann, F., Mancktelow, N. S., Wex, S., Camacho, A. and Pennacchioni, G.: Pseudotachylyte as
443 field evidence for lower-crustal earthquakes during the intracontinental Petermann Orogeny
444 (Musgrave Block, Central Australia), Solid Earth, 9(3), 629–648, doi:10.5194/se-9-629-2018, 2018.

445 Hawemann, F., Mancktelow, N. S., Pennacchioni, G., Wex, S. and Camacho, A.: Weak and slow,
446 strong and fast: How shear zones evolve in a dry continental crust (Musgrave Ranges, Central
447 Australia), Journal of Geophysical Research: Solid Earth, doi:10.1029/2018JB016559, 2019.

448 Hobbs, B.E.: Recrystallisation of single crystals of quartz. Tectonophysics, 6, 353-401, 1968.

449 Hofer, H. E. and Brey, G. P.: The iron oxidation state of garnet by electron microprobe: Its
450 determination with the flank method combined with major-element analysis, American
451 Mineralogist, 92(5–6), 873–885, doi:10.2138/am.2007.2390, 2007.

452 Jamtveit, B., Ben-Zion, Y., Renard, F., Austrheim, H.: Earthquake-induced transformation of the lower
453 crust. Nature 556, 487-491, 2018a.

454   Jamtveit, B., Moulas, E., Andersen, T.B., Austrheim, H., Corfu, F., Petley-Ragan, A., Schmalholz, S.M.:
455   High pressure metamorphism caused by fluid induced weakening of deep continental crust.
456   Scientific Reports, 8, 17011, 2018b.

457   Jamtveit, B., Petley-Ragan,A., Incel, S., Dunkel, K.G., Aupart,C., Austrheim, H., Corfu, F., Menegon, L.,
458   Renard, F: The effects of earthquakes and fluids on the metamorphism of the lower continental
459   crust, Journal of Geophysical Research: Solid Earth, doi:10.1029/2018jb016461, in press.

460   Ji, S., Zhao, P. and Saruwatari, K.: Fracturing of garnet crystals in anisotropic metamorphic rocks
461   during uplift, Journal of Structural Geology, 19(5), 603–620, 1997.

462   Karato, S., Wang, Z., Liu, B. and Fujino, K.: Plastic deformation of garnets: systematics and
463   implications for the rheology of the mantle transition zone, Earth and Planetary Science Letters,
464   130(1–4), 13–30, 1995.

465   Kirkpatrick, J. D. and Rowe, C. D.: Disappearing ink: How pseudotachylytes are lost from the rock
466   record, Journal of Structural Geology, 52, 183–198, doi:10.1016/j.jsg.2013.03.003, 2013.

467   Konrad-Schmolke, M., O'Brien, P. J., Heidelbach, F.: Compositional reequilibration of garnet: the
468   importance of sub-grain boundaries. European Journal of Mineralogy 19, 431–438, 2007.

469   Kunze, K., Wright, S. I., Adams, B. L. and Dingley, D. J.: Advances in automatic EBSP single orientation
470   measurements, Texture, Stress, and Microstructure, 20(1–4), 41–54, 1993.

471   Lasaga, A. C.: Geospeedometry: an extension of geothermometry, in Kinetics and equilibrium in
472   mineral reactions, pp. 81–114, Springer. [online] Available from:
473   http://link.springer.com/chapter/10.1007/978-1-4612-5587-1_3 (Accessed 28 May 2017), 1983.

474   Major, R. B.: Explanatory Notes for the Woodroffe 1: 250 000 Geological Map SG/52-12 (1st
475   ed.). Adelaide, Australia: Geological Survey of South Australia, 1973.

476   Massey, M. A., Prior, D. J. and Moecher, D. P.: Microstructure and crystallographic preferred
477   orientation of polycrystalline microgarnet aggregates developed during progressive creep, recovery,
478   and grain boundary sliding, Journal of Structural Geology, 33(4), 713–730,
479   doi:10.1016/j.jsg.2010.12.009, 2011.

480   Menegon, L., Pennacchioni, G., Malaspina, N., Harris, K., Wood, E.: Earthquakes as precursors of
481   ductile shear zones in the dry and strong lower crust. Geochemistry, Geophysics, Geosystems, 18.
482   https://doi. org/10.1002/2017GC007189, 2017.

483   Papa, S., Pennacchioni, G., Angel, R. J. and Faccenda, M.: The fate of garnet during (deep-seated)
484   coseismic frictional heating: The role of thermal shock, Geology, 46(5), 471–474,
485   doi:10.1130/G40077.1, 2018.

486   Passchier, C.W., Trouw, R.A.J.: Microtectonics (2nd Edition), Springer, Heidelberg, 366 pp., 2005.

487   Petley-Ragan, A., Dunkel, K. G., Austrheim, H., Ildefonse, B., Jamtveit, B.: Microstructural records of
488   earthquakes in the lower crust and associated fluid-driven metamorphism in plagioclase-rich
489   granulites. Journal of Geophysical Research: Solid Earth, 123, 3729–3746.
490   https://doi.org/10.1029/2017JB015348, 2018

491   Petley-Ragan, A., Ben-Zion, Y., Austrheim, H., Ildefonse, B., Renard, F., Jamtveit, B.: Dynamic
492   earthquake rupture in the lower crust. Science Advances, 5, doi: 10.1126/sciadv.aaw0913, 2019.

493   Prior, D. J.: Sub-critical fracture and associated retrogression of garnet during mylonitic deformation,
494   Contributions to Mineralogy and Petrology, 113(4), 545–556, doi:10.1007/BF00698322, 1993.

495   Prior, D. J., Wheeler, J., Brenker, F. E., Harte, B. and Matthews, M.: Crystal plasticity of natural
496   garnet: New microstructural evidence, Geology, 28(11), 1003, doi:10.1130/0091-
497   7613(2000)28<1003:CPONGN>2.0.CO;2, 2000.

498   Prior, D. J., Wheeler, J., Peruzzo, L., Spiess, R. and Storey, C.: Some garnet microstructures: an
499   illustration of the potential of orientation maps and misorientation analysis in microstructural
500   studies, Journal of Structural Geology, 24(6–7), 999–1011, doi:10.1016/S0191-8141(01)00087-6,
501   2002.

502   Raimondo, T., Collins, A. S., Hand, M., Walker-Hallam, A., Smithies, R. H., Evins, P. M. and Howard, H.
503   M.: The anatomy of a deep intracontinental orogen, Tectonics, 29(4), n/a-n/a,
504   doi:10.1029/2009TC002504, 2010.

505   Shimada, M., Cho, A., Yukutake, H.: Fracture strength of dry silicate rocks at
506   high confining pressures and activity of acoustic emission. Tectonophysics 96, 159–
507   172. doi:10.1016/0040-1951(83)90248-2, 1983.
508

509   Sibson, R. H.: Generation of pseudotachylyte by ancient seismic faulting, Geophysical Journal
510   International, 43(3), 775–794, 1975.

511   Sibson, R. H. and Toy, V. G.: The habitat of fault-generated pseudotachylyte: Presence vs. absence of
512   friction-melt, in Geophysical Monograph Series, vol. 170, edited by R. Abercrombie, A. McGarr, H.
513   Kanamori, and G. Di Toro, pp. 153–166, American Geophysical Union, Washington, D. C. [online]
514   Available from: http://www.agu.org/books/gm/v170/170GM16/170GM16.shtml (Accessed 21
515   January 2014), 2006.

516   Toy, V. G., Ritchie, S. and Sibson, R. H.: Diverse habitats of pseudotachylytes in the Alpine Fault Zone
517   and relationships to current seismicity, Geological Society, London, Special Publications, 359(1), 115–
518   133, doi:10.1144/SP359.7, 2011.

519   Trepmann, C. A. and Stöckhert, B.: Cataclastic deformation of garnet: a record of synseismic loading
520   and postseismic creep, Journal of Structural Geology, 24(11), 1845–1856, doi:10.1016/S0191-
521   8141(02)00004-4, 2002.

522   Voegelé, V., Cordier, P., Sautter, V., Sharp, T. G., Lardeaux, J. M. and Marques, F. O.: Plastic
523   deformation of silicate garnets, Physics of the Earth and Planetary Interiors, 108(4), 319–338,
524   doi:10.1016/S0031-9201(98)00111-3, 1998.

525   Vollbrecht, A., Pawlowski, J., Leiss, B., Heinrichs, T., Seidel, M. and Kronz, A.: Ductile deformation of
526   garnet in mylonitic gneisses from the Münchberg Massif (Germany), Tectonophysics, 427(1–4), 153–
527   170, doi:10.1016/j.tecto.2006.05.024, 2006.

528   Wang, Z. and Ji, S.: Deformation of silicate garnets; brittle-ductile transition and its geological
529   implications, The Canadian Mineralogist, 37(2), 525, 1999.

530   Wayte, G. J., Worden, R. H., Rubie, D. C. and Droop, G. T. R.: A TEM study of disequilibrium
531   plagioclase breakdown at high pressure: the role of infiltrating fluid, Contributions to Mineralogy
532   and Petrology, 101(4), 426–437, doi:10.1007/BF00372216, 1989.

533 Wex, S., Mancktelow, N. S., Hawemann, F., Camacho, A. and Pennacchioni, G.: Geometry of a large-
534 scale, low-angle, mid-crustal thrust (Woodroffe Thrust, central Australia): Geometry of a mid-crustal
535 thrust, Tectonics, doi:10.1002/2017TC004681, 2017.

536 Wex, S., Mancktelow, N. S., Hawemann, F., Camacho, A. and Pennacchioni, G.: Inverted distribution
537 of ductile deformation in the relatively "dry" middle crust across the Woodroffe Thrust, central
538 Australia, Solid Earth, 9(4), 859–878, doi:10.5194/se-9-859-2018, 2018.

539 Wex, S., Mancktelow, N. S., Camacho, A. and Pennacchioni, G.: Interplay between seismic fracture
540 and aseismic creep in the Woodroffe Thrust, central Australia – Inferences for the rheology of
541 relatively dry continental mid-crustal levels, Tectonophysics, 758, 55–72,
542 doi:10.1016/j.tecto.2018.10.024, 2019.

543

544

545

546

547

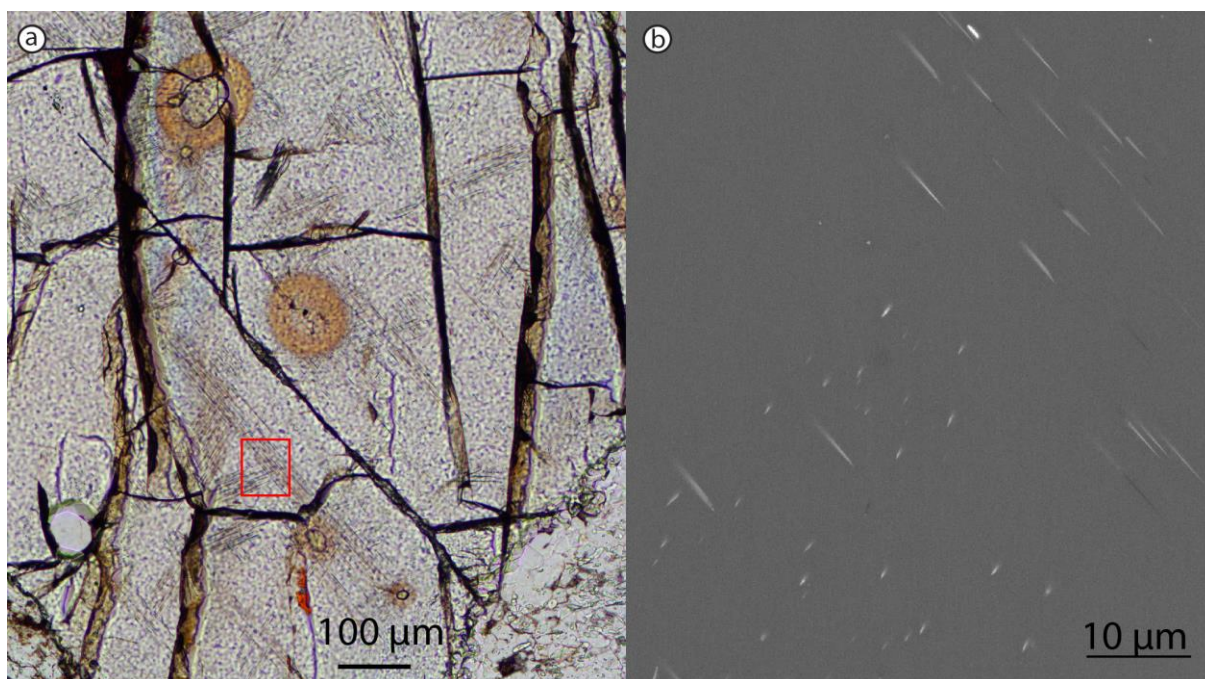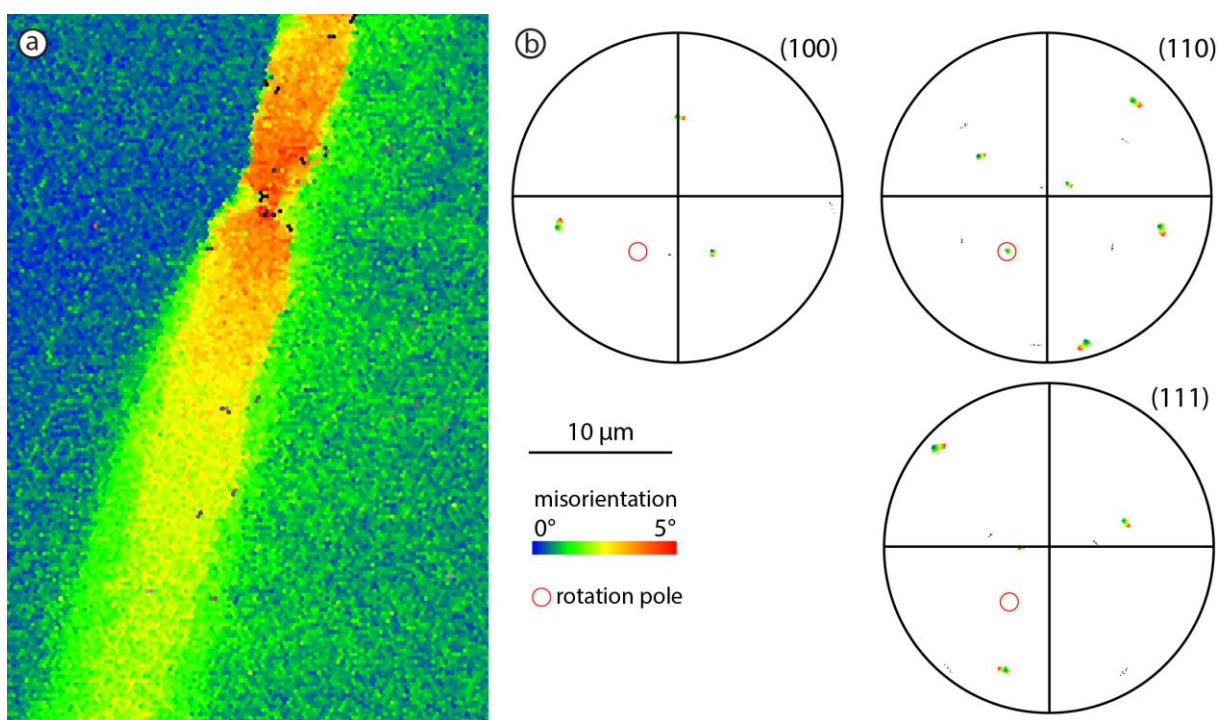548

549

550 **Appendix**

551

Figure A1: Thin section image in plane polarized light of a garnet crystal with monazite inclusions (with halos) and rutile-exsolution needles. b) BSE-image of the area indicated with the red box.

555

556   *Figure A2: a) Misorientation map-detail for Fig. 6b), with b) pole figure plots for garnet axis*

557   *with the same colour scheme. The plots reveal a rotation around a (101)-axis, as indicated by*

558   *the red circle.*